Materials Today Advances 30 (2026) 100805

Contents lists available at ScienceDirect

Materials Today Advances

journal homepage: www.sciencedirect.com/journal/materials-today-advances/

Hidden topological number of quadratic Dirac fermions in β-PbO_2

Chin-Shen Kuo [a,1], Angus Huang [a,1], Chin-Hsuan Chen [a], Horng-Tay Jeng [a,b,c,d,*]

[a] Department of Physics, National Tsing Hua University, Hsinchu 30013, Taiwan
[b] Physics Division, National Center for Theoretical Sciences, Taipei 10617, Taiwan
[c] Institute of Physics, Academia Sinica, Taipei 11529, Taiwan
[d] Research Center for Semiconductor Materials and Advanced Optics, Chung Yuan Christian University, Taoyuan 32031, Taiwan

ARTICLE INFO

Keywords:
Dirac
DFT
PbO2
Topological matter

ABSTRACT

Gapless topological phase, including Weyl, Dirac, and nodal line semimetals, has become an attractive research field in recent years. Some of them have been studied in elementary particle physics, while nodal line and quadratic Dirac semimetals are beyond. Among the latter category, nodal line semimetals have been well studied in the past decade, however, the quadratic Dirac semimetals are less discovered by experiments or first-principles calculations, and how to analyze the topological properties of a Dirac node itself remains elusive while highly desirable. In this work, we developed a new method to unravel a hidden topological invariance of quadratic Dirac fermion of β-PbO_2. Through density functional theory (DFT) and $\mathbf{k}\cdot\mathbf{p}$ model in this new approach, we predict that β-PbO_2 hosts the quadratic Dirac node (QDN) with mirror Chern number 2 when spin–orbit coupling is included, surpassing previous studies of topological semimetals. Our work paves the route toward a new class of topological matter.

1. Introduction

Classification of topological phases is an important issue for both solid state and elementary particle physics. Distinct topological phases are classified by different topological invariants, where the emerging quasi-particles can be an analog of elementary particles. Specifically, in Weyl semimetals (WSMs) [1–4], Dirac semimetals (DSMs) [5–13], axion materials [14], and topological superconductors [15–19], the low-energy excitations are in direct correspondence with the Weyl, Dirac, axion, and Majorana fermions, respectively. Moreover, the quasi-particles that are beyond study of particle physics, such as type II Weyl [20–23], type II Dirac [24–26], and nodal line Fermions [27–31] have been found also. Topological materials with topological invariant numbers (Chern numbers or Z_2 invariant numbers) exhibit topologically protected surface states robust to perturbations. Interestingly, some of them present high Chern number ≥ 2, for example, three-component [32–38], double or triple Weyl fermions [39–41], Dirac semimetal with Chern number 2 [42].

In addition, it was predicted that rotational invariant crystals can realize the so-called double or triple Weyl fermions [39–41]. In contrast to the typical Weyl fermions with linear energy dispersion in all directions, multi-Weyl fermions characterized by quadratic or cubic in-plane energy dispersions lead to exotic physical properties such as non-Fermi liquid due to the enhancement in the density of states [41,43,44]. On the other hand, if inversion and time-reversal symmetry also present in the system, then a pair of multi-Weyl fermions with opposite charity will couple into Dirac fermion. A family of transition-metal chalcogenide compounds was firstly reported [45] to host such Dirac fermion with cubic in-plane energy dispersion composed of a pair of triple Weyl fermions. A quadratically dispersed Dirac fermion is also found in the same system with the energy far above the Fermi level [45], which would be difficult to be confirmed by, e.g., angle-resolved photoemission spectroscopy (ARPES) experiments. While the quadratic Dirac cone proposed in α-TeO_2 [46] far below the Fermi level may be easier to be observed in future experiments.

In previous studies on Dirac semimetals, the topological surface states are typically considered with time-reversal Z_2 topological number or mirror Chern numbers [47,48]. Contrarily, studies on topological materials protected by rotational symmetry such as the topological numbers in bismuth (Bi) [49] are rare. Unlike Weyl semimetals, where the topological number can be directly calculated from the Weyl nodes [50,51], studies on topological numbers of rotational symmetry protected Dirac semimetals focus on other parts of the band structure, such as the time-reversal invariant points or mirror planes [47,48], while the topological numbers of the Dirac nodes themselves has not been thoroughly investigated.

* Corresponding author at: Department of Physics, National Tsing Hua University, Hsinchu 30013, Taiwan.
E-mail address: jeng@phys.nthu.edu.tw (H.-T. Jeng).
[1] Contributed equally to this work.

https://doi.org/10.1016/j.mtadv.2026.100805
Received 22 January 2026; Received in revised form 16 April 2026; Accepted 2 May 2026
Available online 12 May 2026

Lead oxide has been widely used in lead–acid battery electrodes with the main component of β-PbO_2 for over 100 years. The topological phase of β-PbO_2, which shares the same rutile structure as β'-PtO_2, has been presented in previous studies [52–55]; however, the topological numbers of the Dirac nodes themselves and topological surface states of β-PbO_2 have not been carefully investigated to date. In this work, using *ab initio* calculations, we explore the topological properties of β-PbO_2 and its associated topological numbers. We present that β-PbO_2 exhibits a pair of nodal rings intersecting at two nexus points in non-spin–orbit coupling (non-SOC) calculations. Furthermore, when SOC is included, it can host Dirac fermions with quadratic in-plane energy dispersion protected on the four-fold rotation axis arond the Fermi level, which is suitable for experimental examination. Combining with a $k \cdot p$ model, we reveal that a pair of weakly coupled double Weyl fermions constitute this Dirac fermion of β-PbO_2, for which the in-plane quadratic dispersion depends crucially on the coupling strength of SOC. These newly discovered bulk and surface electronic properties make β-PbO_2 very distinct from the typical DSMs such as Na_3Bi [10] and Cd_3As_2 [5], leading to a new class of topological materials.

2. Methods

First-principles calculations are performed using the Vienna Ab initio Simulation Package (VASP) with projector augmented wave (PAW) [56–58] pseudopotential based on the density functional theory (DFT). Perdew–Burke–Ernzerhof (PBE) [59] type generalized gradient approximation (GGA) exchange–correlation functional with energy cutoff of 400 eV are used in this work. In comparison with experimental lattice parameters: a = b = 4.9554 Å and c = 3.3861 Å, the theoretically optimized lattice parameters a = b = 5.0004 Å and c = 3.4337 Å are very close to the experimental values (~1%). Heyd–Scuseria–Ernzerhof hybrid functional (HSE03 and [60,61] HSE06 [62]) and modified Becke–Johnson (mBJ) [63,64], calculations are also carried out for comparison with the energy band gaps. 18 × 18 × 24 **k**-point samplings are used in PBE-type GGA functional calculations. While 8 × 8 × 12 and 4 × 4 × 8 k-point meshes are used in mBJ and HSE03(HSE06) calculations, respectively. The Wannier functions with Pb *s* and O *p* orbitals are projected from DFT results to calculate the hopping parameters. The surface state spectra are constructed from semi-infinite slab method [65] with the Wannier functions. The group representations are extracted from the eigenvalues of symmetry operators from Wannier functions and DFT wavefunctions. The $k \cdot p$ model and topological invariance are obtained from the hopping parameters of Wannier basis.

3. Results and discussion

3.1. Bulk properties without SOC

As shown in Fig. 1(a), β-PbO_2 crystallizes in the rutile structure with space group $P4_2/mnm$ (#136, D_{4h}^{14}) containing the screw rotational ($\hat{C}_4$), mirror ($\hat{M}_{001}$, $\hat{M}_{110}$, $\hat{M}_{\bar{1}10}$), inversion ($\hat{P}$), and time-reversal ($\hat{T}$) symmetry. Similar to other carbon group oxides AO_2 (A=Si, Ge, Sn) in the rutile structure [66], the conduction band (CB) and valence band (VB) of β-PbO_2 also show an electron and a hole pocket corresponding to the single [double] point group representations Γ_1^+ [Γ_6^+] and Γ_3^+ [Γ_7^+], respectively, at the Brillouin zone (BZ) (Fig. 1(b)) center. However, instead of the two gaped pockets of other carbon group rutile oxides, β-PbO_2 exhibits crossing electronic band structures. When SOC is ignored, this crossing presents a pair of nodal rings in the $(\bar{1}10)$ and (110) plane. Fig. 1(c) shows the two-dimensional band structure on the $(\bar{1}10)$ plane, on which the CB and VB do not hybridize with each other due to different mirror $\hat{M}_{\bar{1}10}$ eigenvalues, +1 (−1), respectively. The CB and VB cross into approximately an ellipse, therefore realizing a nodal ring on the $(\bar{1}10)$ plane. Moreover, due to $\hat{C}_4$ symmetry, there is another equivalent nodal ring on the perpendicular (110) plane, which intersects

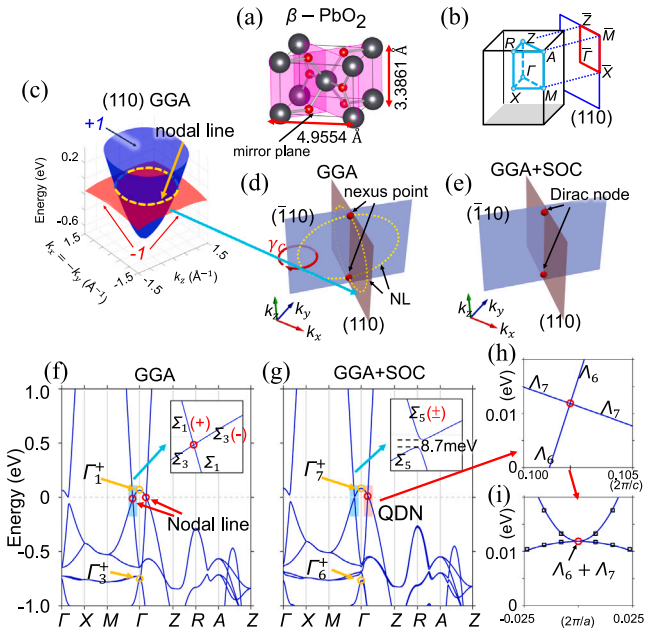

Fig. 1. Lattice structure and bulk band structure of β-PbO_2 (a) Rutile structure of β-PbO_2. (b) Brillouin zone of β-PbO_2. (c) Nodal line band structure in (110) plane. The bands with different mirror eigenvalues are show in different color and the dash line indicates the nodal ring protected by mirror symmetry. (d) and (e) The sketch of gapless point without and with SOC, respectively. (f) and (g) GGA (PBE) band structure without and with SOC, respectively. The plus and minus signs (±) indicate the mirror eigenvalues. (h) Zoom-in band structure along $\Gamma - Z$ (Λ) from GGA+SOC. (i) Three dimensional DN band structure along the direction perpendicular to $\Gamma - Z$ (Λ) from GGA+SOC. The quadratic behavior can be seen clearly. (For interpretation of the references to color in this figure legend, the reader is referred to the web version of this article.)

the $(\bar{1}10)$ plane nodal ring at two nexus points along the rotation axis (i.e., k_z axis) in Fig. 1(d). The nodal ring states can be identify from the band structure along the high-symmetry paths from GGA (Fig. 1(f)), where a pair of concave up and concave down parabolic cones around the Γ point cross each other at the Fermi level forming the gapless nodal line as indicated by the red arrows. As a result, the electron pocket around Γ crosses the hole pocket at two points along $\Gamma \to M$ and $\Gamma \to Z$. Both the two paths are on the $(\bar{1}10)$ plane; particularly, the gapless point along $\Gamma \to Z$ is the nexus point at which the pair of nodal rings intersect.

The stability of the nodal rings can be studied from the topological point of view. We classify the nodal rings of β-PbO_2 by two topological invariants: the mirror index n_+ [28] and the Berry phase γ_C. Precisely, the mirror index $n_+ \in \mathbb{Z}$ counts the mirror eigenvalues of the occupied states separated by the line node. Whereas the Berry phase $\gamma_C = \int_C A(\mathbf{k}) \cdot d\mathbf{k}$ is the integral of Berry connection along a loop C (Fig. 1(d)) that encircles the line node, which quantizes to $\gamma_C = 0, \pi \,(\mathrm{mod}\, 2\pi)$ since $\hat{P}$, $\hat{T}$ and $SU(2)$ spin rotation symmetry [67]. For the nodal rings of β-PbO_2, we found $n_+ = 1$ and $\gamma_C = \pi$, where the Berry phase was calculated using the effective tight-binding model. The nodal rings are protected by these nontrivial topological invariants emerging from different symmetries: n_+ originates from the mirror symmetry ($\hat{M}_{\bar{1}10}$ or $\hat{M}_{110}$), while the quantization in γ_C is due to $\hat{P}$, $\hat{T}$ and $SU(2)$. Therefore, the nodal rings shall remain intact unless certain perturbation violates these symmetries at the same time. Moreover, the seemingly unrelated n_+ and γ_C are indeed related through

$$n_+ = \gamma_C/\pi \mod 2 \tag{1}$$

which implies γ_C is trivial (non-trivial) if n_+ is even (odd).

We also construct a $k \cdot p$ model to describe the low-energy behavior of β-PbO_2 without the inclusion of SOC. We introduce a set of Pauli matrices τ_i $(i = 0, x, y, z)$ to describe the states Γ_1^+ and Γ_3^+ at the BZ center, which correspond to the CB and VB respectively. Then, constrained by D_{4h} and $\hat{T}$, the Hamiltonian uniquely takes the form (to second order in $\mathbf{k}$)

$$H_{\text{noSOC}}(\mathbf{k}) = M(\mathbf{k})\tau_0 + M'(\mathbf{k})\tau_z + B_1(k_x^2 - k_y^2)\tau_x \tag{2}$$

where $M(\mathbf{k}) = M_0 + M_1 k_z^2 + M_2(k_x^2 + k_y^2)$ and $M'(\mathbf{k}) = M_0' + M_1' k_z^2 + M_2'(k_x^2 + k_y^2)$ with real coefficients. This model describes a pair of nodal rings around the BZ center. On either $(\bar{1}10)$ or (110) plane where $|k_x| = |k_y|$, the off-diagonal terms vanish due to the mirror symmetry, which results in a nodal ring described by the ellipse $(-2M_2'/M_0')k_x^2 + (-M_1'/M_0')k_z^2 = 1$.

3.2. Bulk properties with SOC: Quadratic Dirac nodes

With SOC taken into consideration, the nodal ring state without SOC along $\Gamma \to M$ (Fig. 1(f) and inset) opens a gap ~ 9 meV throughout the nodal ring by SOC as can be seen in the light blue region and the inset of Fig. 1(g), except the crossing along $\Gamma \to Z$ between Λ_6 and Λ_7 in the light red region, forming the QDN as further demonstrated in Fig. 1(h,i). The QDN remain gapless with SOC due to the protection from time-reversal and inversion symmetry, which ensures double degeneracy. The fourfold (quadratic) degeneracy is maintained by the crystal group symmetry, thus the inclusion of SOC cannot open a gap at the Dirac point. As a result, the Dirac node is positioned exactly at the Fermi level, indicating a robust symmetry-protected degeneracy. Meanwhile, quadratic Dirac nodes emerge in β-PbO_2 (Fig. 1(i)). The SOC violates SU(2) spin rotational symmetry and this symmetry breaking gaps out the nodal ring (Fig. 1(g)). However, the pair of nexus points on k_z could be preserved by $\hat{C}_4$ rotational symmetries, as shown in Fig. 1(e), (g)–(i). Close to these DNs, the bands disperse linearly along k_z (Fig. 1(g)) like reported in most DSMs such as Na_3Bi [10] and Cd_3As_2 [5]. In contrast, we observe quadratic dispersion on the perpendicular $k_x - k_y$ plane, as demonstrated by Fig. 1(i) with a quadratic fitting. It is the first time that a DN with quadratic in-plane dispersion is reported in real material with four-fold rotational symmetry.

To explain the quadratic DNs, we extend the $k \cdot p$ Hamiltonian to including the SOC. Here we use the Pauli matrices σ_i to represent the spin degree of freedom, the 4×4 Hamiltonian satisfying $\hat{D}_{4h}$ and $\hat{T}$ will take the form (to the second order in $\mathbf{k}$)

$$\begin{aligned} H_{\text{SOC}}(\mathbf{k}) = {} & H_{\text{noSOC}}(\mathbf{k}) \otimes \sigma_0 - B_2 k_x k_y \tau_y \otimes \sigma_z \\ & + A k_z (k_x \tau_y \otimes \sigma_y + k_y \tau_y \otimes \sigma_x). \end{aligned} \tag{3}$$

where real numbers A and B_2 represent the SOC strength and all parameters are summarized in Table 1. It can be seen that A and B_2, which accounts for SOC in PbO_2, plays minor roles only as compared to B_1. Although SOC is expected to be strong in heavy atom Pb, the major contributions to CB and VB come from the light O ions, whereas Pb only contribute 0.5% (<0.1%) to the CB (VB) at Γ point, Consequently, the Hamiltonian $H_{\text{SOC}}(\mathbf{k})$ describes a pair of Weyl nodes (WN)

$$H_{\pm}(\mathbf{k}) = M(\mathbf{k})\tau_0 + M'(\mathbf{k})\tau_z + B_1(k_x^2 - k_y^2)\tau_x \pm B_2 k_x k_y \tau_y \tag{4}$$

with the trivial SOC component Ak_z neglected. The $H_{\pm}(\mathbf{k})$, which map to each other by $\hat{T}$, describe the Weyl semimetals (WSMs) hosting a pair of double WNs at $\pm k_z' = \pm\sqrt{-M_0'/M_1'}$. To demonstrate, we plot in Fig. 2a and b the Berry curvature associated with the occupied states. Both resemble magnetic dipoles: for $H_-(\mathbf{k})$ ($H_+(\mathbf{k})$), the Berry curvature flows out from the double WN at $-k_z'$ ($+k_z'$) with Chern number $C = +2$; then flows into the other node at the $+k_z'$ ($-k_z'$) with $C = -2$. These double WNs are protected by $\hat{C}_4$ on the rotation axis k_z, with quadratically dispersed bands on the k_x-k_y plane [39,41]. At either $\pm k_z'$, two double WNs with opposite Chern numbers then couple into a DN. As the coupling barely contributes to the band dispersion, this explains the quadratic behavior observed in our DFT result of β-PbO_2.

Table 1
The $k \cdot p$ parameters calculated from the tight-binding model. To improve the quality of the perturbation result, we have reduced the lattice constant c by 3% so that the Γ_6^+ state could be shifted away from those strongly interacting lower occupied states.

Parameters	Values
M_0 (M_0')	−0.137 (−0.206) eV
M_1 (M_1')	11.825 (13.806) eV A^2
M_2 (M_2')	12.516 (15.295) eV A^2
B_1 (B_2)	−1.887 (−0.382) eV A^2
A	−0.487 eV A^2
k_z'	0.122 (A^{-1})

Eq. (4) describes an isotropic double-Dirac node with quadratic band dispersion in the xy-plane. To further demonstrate this fact, we perform DFT band structure calculations passing the Dirac point along (100), (010), (110), and $(1\sqrt{3}0)$ directions on the xy-plane as shown in Supplementary Figs. S7(a–d), respectively. Clearly, the quadratic Dirac band dispersion is isotropic in all directions on the xy-plane, with no directional dependence in the band velocities and effective mass. In addition, the nodal point exhibits a four-fold degeneracy, which illustrates a defining characteristic of a double-Dirac point. This is further supported by the 3-dimensional plot of the Dirac cone in Supplementary Fig. S8, which shows the isotropic Dirac cone dispersion over the xy-plane.

Notice that the Berry curvature is opposite for $H_{\mp}(\mathbf{k})$ (due to $\hat{P}\hat{T}$), which implies vanishing Chern number for the DNs. However, on the $k_z = 0$ plane, $H_{\mp}(\mathbf{k})$ strictly decouple from each other owing to the mirror symmetry $\hat{M}_{001}$ (represented by $-i\tau_0 \otimes \sigma_z$). Remarkably, such decoupled Berry flux on the $k_z = 0$ plane indicates a nontrivial mirror Chern number $C_m = -2$ for the system. Our observation here, in fact, contradicts the prediction made by Ref. [44], saying that DNs with quadratic in-plane dispersion only exist in crystals satisfying C_6 but not C_4 like β-PbO_2. This controversy is due to the ambiguity in determining the dominating term of a model Hamiltonian. For our model (Eq. (5)), we have identified $H_-(\mathbf{k}) \oplus H_+(\mathbf{k})$ as an unperturbed Hamiltonian, which describes double WNs with quadratic in-plane dispersion

$$E(k_x, 0, k_z') \simeq \begin{cases} 27.926 k_x^2 \text{ eV} & \text{for upper cone} \\ -2.894 k_x^2 \text{ eV} & \text{for lower cone.} \end{cases} \tag{5}$$

whereas the coupling $Ak_z'(k_x\tau_y\sigma_y + k_y\tau_y\sigma_x)$, as a perturbation, contributes linear energy shift

$$\Delta E(k_x, 0, k_z') = \pm(Ak_z')k_x = \pm 0.059 k_x \text{ eV}, \tag{6}$$

from which we can conclude that the energy dispersion is dominated by the quadratic terms except for $(k_x, k_y) \to (0, 0)$. We note that the dispersion must be linear whenever the coupling do not vanish exactly. Furthermore, since the quadratic and linear terms compete with each other, we propose the idea of tunable-quadratic Dirac node (TQDN), whose in-plane energy dispersion can be tuned from quadratic to linear (or vice versa) by physical parameters. We demonstrate this idea in Fig. 2c–d, where we increase either A or k_z' (position of the DN) so that the bands disperse more linearly on the k_x-k_y plane. Physically, for β-PbO_2, parameter A corresponds to the SOC strength which can be modulated by, for example, doping.

3.3. Surface state

To confirm the topological properties, the surface states of β-PbO_2 are demonstrated in Fig. 3. For (110) surface without SOC, the nodal line forms a ring parallel to the surface surrounding $\bar{\Gamma}$ (Fig. 3(b)) with a gapless point in $\bar{\Gamma} \to \bar{X}$ direction, as highlighted by a red point in Fig. 3(a). On the other hand, the nodal ring hosted in another plane, $(1\bar{1}0)$,

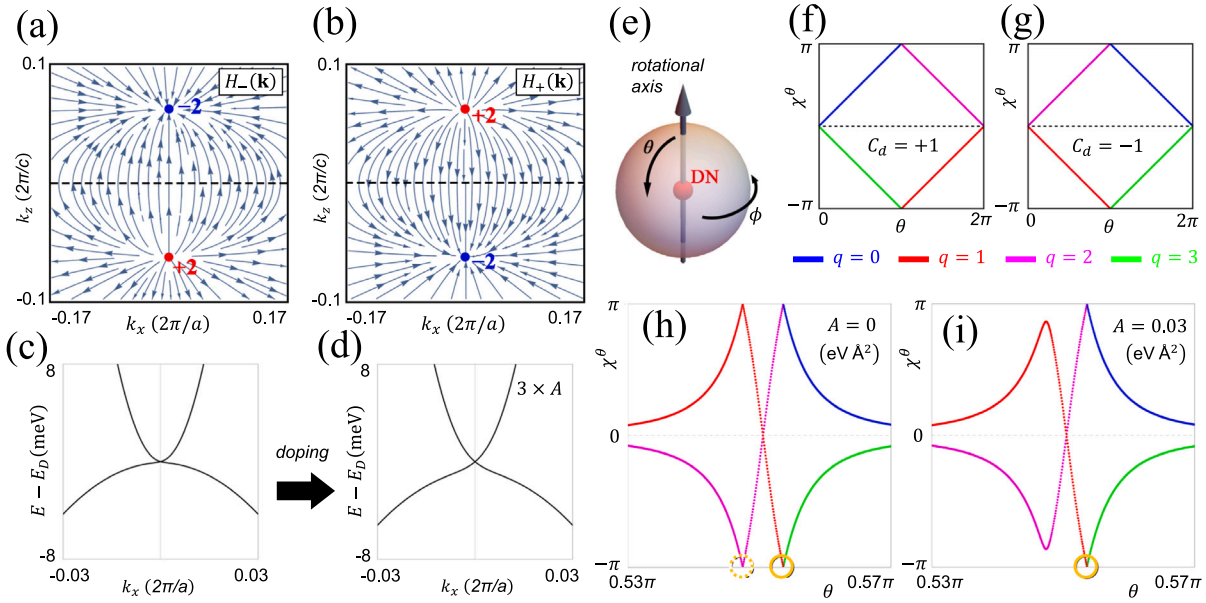

Fig. 2. (a) (b) The Berry curvature of $H_{\pm}(\mathbf{k})$ on the k_x-k_z plane. The red (blue) dot indicates the position of the double WN with $C = +2$ (-2). The horizontal dashed line is the projection of the $k_z = 0$ plane. (c) (d) Demonstration of the QDN, where E_D is the energy of the DN. (e) Illustration of the Wilson loop method (see Supplementary Figures S1 and discussion for detail). We enclose the DN (red dot) protected on the C_4 rotation axis by a sphere. At polar angle θ, the Wilson loop $\mathcal{W}^{\theta}_{0\to 2\pi}$ is defined as the non-abelian Berry phase of the adiabatic evolution from $\phi = 0$ to $\phi = 2\pi$ in azimuthal direction. The phases of these $\mathcal{W}^{\theta}_{0\to 2\pi}$ eigenvalues are called the Wilson energy $\chi^{\theta} \in [-\pi, \pi)$. By plotting χ^{θ} against $0 \le \theta \le \pi$, the Wilson spectrum is obtained, which provides the basis for the topological classification. Moreover, each band on the Wilson spectrum is distinguished by the quantum number $q \in \{0, 1, 2, 3\}$, with different color, owing to the rotation symmetry. (f) (g) The two and the only two possible Wilson spectra dictated by symmetries. We say that the DN has topological charge $C_d = +1$ or -1 if its Wilson spectrum is equivalent to (f) or (g). (h) (i) The Wilson spectrum for the DN of β-PbO_2 at k'_z without and with the coupling between the WNs. The solid (dashed) circle indicates the protected (unprotected) crossing. For protected crossings, the crossing bands are associated with different quantum numbers, so which cannot be gapped out by symmetry-preserving perturbation on the Hamiltonian. (For interpretation of the references to color in this figure legend, the reader is referred to the web version of this article.)

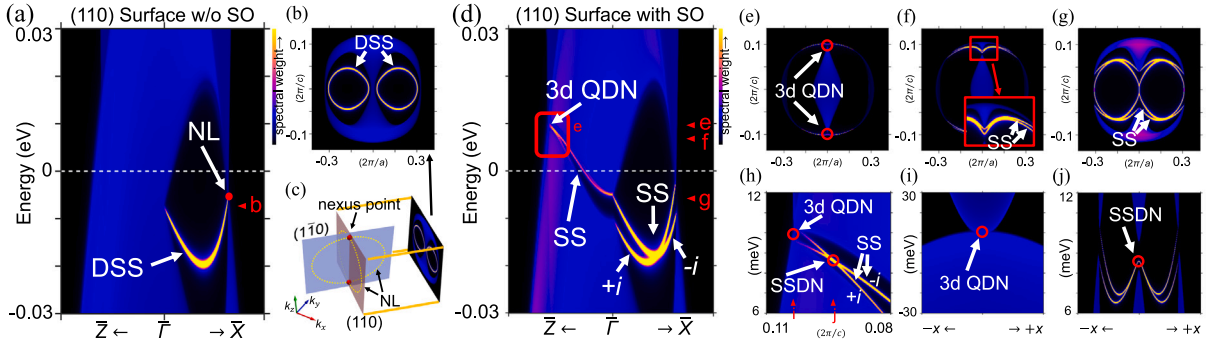

Fig. 3. The surface states of β-PbO_2. (a) The (110) surface spectrum without SOC summing over bulk states and surface states. The red arrow indicate the energy level of sub-figure (b). (b) The 2-d energy contour in (110) surface within the energy range $E = [-0.01, -0.008]$ eV. (c) The nodal lines in (110) and $(1\bar{1}0)$ are indicate by yellow dotted circles and the nexus points are labeled by red points. (d) The surface states in (110) surface with SOC included. The original QDN is in the red rectangle. The original topological drumhead surface states split and become the topological surface states, protected by mirror symmetry of (001) mirror plane. (e)(f) 2-d contours at and near the QDN with the energy indicated by the corresponding red arrows in (d), respectively. (g) 2-d contours of surface states in (001) plane at energy indicated by the corresponding red arrow in (d). (h) Zoom-in plot of (d) around the QDN. Another pair of topological surface states are demonstrated with the surface state Dirac node (SSDN) protected by the mirror symmetry of $(1\bar{1}0)$. (i)(j) Zoom in QDN and SSDN along anther perpendicular direction of (d), respectively. (For interpretation of the references to color in this figure legend, the reader is referred to the web version of this article.)

along $\bar{\Gamma} \to \bar{Z}$ direction are metallic. These projections of two nodal rings form a Θ-shaped 2-d constant energy contour (blue), as shown in Fig. 3b. Moreover, each (110) nodal ring contact with a drumhead surface state (DSS) (Fig. 3(c)), consistent with our calculations of n^+ and γ_C.

When SOC is included, the gapless nodal ring state in (110) surface along $\bar{\Gamma} \to \bar{X}$ direction splits, as shown in Fig. 3(d). In $\bar{\Gamma} \to \bar{Z}$ direction, the gapless bulk bands open a small continuous band gap except the projected QDN point. From the 2-d contours in Fig. 3(e) and (f), the Θ sharp bulk bands split into the conduction band and valence band and connect each other at the 3-d QDN. On the other hand, the paraboloid drumhead surface states in the non-SOC case split into two stacking paraboloid surface states (Fig. 3g) and touch each other at the surface state DN (SSDN). The mirror eigenvalues $\pm i$ of the surface states with respect to the (001) mirror plane shown in Fig. 3(d) illustrate the mirror symmetry protected SSDN. Interestingly, this mirror symmetry protected topological surface states are surrounded by the gap away from the QDN and carry the mirror Chern number $n_M = 2$, same as our calculated results above. Moreover, another pair of topological surface states emerge in the SOC gap near the QDN as shown in Fig.

3(h) and (i). From the mirror eigenvalue of these surface states (Fig. 3(h)), we demonstrate they are topological and protected by mirror symmetry of the $(1\bar{1}0)$ plane, even though the mirror Chern numbers are ill-defined because the QDN are gapless points in the $(1\bar{1}0)$ and (110) planes. This Dirac cone of the surface state near the QDN breaks the Lorentz invariance. Moreover, it is a new class of fermion because it shows two positronic fermions properties in the direction perpendicular to $\bar{\Gamma} \rightarrow \bar{Z}$ (Fig. 3(j)), instead of the normal Dirac cones combined electron and hole. Inspired by the studies of type II Weyl [20–23] and Dirac semimetals [24–26], the breaking Lorentz invariance is important because it is beyond particle physics and exhibits strange transport properties. Therefore, the similar character of type II Weyl semimetals may appear in the surface state of β-PbO_2.

3.4. wilson spectrum of a sphere enclosing the Dirac node

From the topological aspect, the in-plane dispersion around a DN can be continuously tuned between quadratic and linear, even though it is not the case for WNs. The WNs protected by the C_4 rotational symmetry are distinguished by Chern number [39], therefore, a single WN ($C = \pm 1$) with linear in-plane dispersion cannot transform continuously into a double WN ($C = \pm 2$) with quadratic dispersion. In contrast, there is only one type of C_4 protected DNs, which is associated with the topological charge $C_d = \pm 1$. This fact has been proved in Supplementary Figure S2 and Section "CLASSIFICATION BY THE WILSON SPECTRUM", where we present a complete classification of C_4 protected DNs based on the Wilson loop method [68–71]. Our approach considers the occupied states on the sphere enclosing the DN (see Fig. 2e), for which the Wilson loop $\mathcal{W}^{\theta}_{0\rightarrow 2\pi}$ at polar angle $0 \le \theta \le \pi$ is defined as the non-abelian Berry phase of the adiabatic evolution from $\phi = 0$ to $\phi = 2\pi$ in azimuthal direction. We refer to the plot of these $\mathcal{W}^{\theta}_{0\rightarrow 2\pi}$ eigenvalues against θ in Fig. 2(f,g,h,i) as the Wilson spectra. Most importantly, symmetries classify Wilson spectra into two categories as presented in Fig. 2(f) and (g). The topological charge of a DN is accordingly defined by $C_d = +1$ ($C_d = -1$) if its Wilson spectrum is equivalent to Fig. 2(f) (Fig. 2(g)). Note that DNs with $C_d = \pm 1$ are indistinguishable except that the rotation eigenvalues exchange at the two poles of the sphere.

For the $k \cdot p$ model of β-PbO_2 (Eq. (3)), we show in Fig. 2(h) the Wilson spectrum of the DN at $+k_z'$ with vanishing coupling (i.e., $A = 0$ for the parameter). Interestingly, the result displays two band crossings, which are marked by dashed- and solid-line circle. It is expected since the DN is decoupled into a pair of double WNs whenever $A = 0$. However, the crossing marked by the dashed-line circle is unstable, which gaps out after switching on the coupling, as presented in Fig. 2(i). Therefore, one could transform Fig. 2(h) continuously into Fig. 2(i), suggesting that the DN at $+k_z'$ is associated with the topological charge $C_d = -1$; while the DN at the opposite k has $C_d = +1$ so that the total charge is neutralized. Besides, the crossing point marked by the solid-line circle in Fig. 2(h,i) is indeed protected by the $\hat{C}_4$ symmetry, which thus remains gapless for any coupling strength. Significantly, such protected crossing in the Wilson spectrum also manifests the topological non-triviality of the DN. To further confirm that this Dirac node is protected by the $\hat{C}_4$ symmetry, we perform DFT band structure calculations under strain with/without the $\hat{C}_4$ symmetry. As shown in Supplementary Figures S5 and S6, the topological DN remains gapless under strain with $\hat{C}_4$ symmetry. In contrast, only 1% of strain without $\hat{C}_4$ symmetry would lead to topologically trivial gaped-DN. Our DFT results demonstrate unambiguously the robust Dirac topology protected by $\hat{C}_4$ symmetry.

The Wilson spectrum for characterizing the topological DN is formulated as follows. We first enclose the DN by a sphere centered at the node, where the radius R is small enough such that the electronic states inside the sphere can be described by a minimal 4×4 $k \cdot p$ model. We denote $|u_{(\theta,\phi),n}\rangle$ as the eigenstate of this minimal model at

$$\mathbf{k} = \mathbf{k}_D + (R\sin\theta\cos\phi, R\sin\theta\sin\phi, R\cos\theta), \tag{7}$$

where $\mathbf{k}_D$ is the position of the DN and $n = 1, 2, 3, 4$ is the band index. Here $|u_{(\theta,\phi),n}\rangle$ is the eigenstate on the enclosing sphere with polar angle $0 \le \theta \le \pi$ and azimuthal angle $0 \le \phi \le 2\pi$. Also, we denote $\hat{C}_4$ (four-fold rotation) and $\widehat{\mathcal{TP}}$ (inversion combined with time-reversal) for the symmetry operators acting on the Hilbert space of the minimal model. The band $n = 1$ and 2 are assumed to be occupied, for which we define the projector by

$$\hat{P}_{(\theta,\phi)} = \sum_{n=1}^{2} |u_{(\theta,\phi),n}\rangle\langle u_{(\theta,\phi),n}|, \tag{8}$$

and the Wilson loop operator

$$\hat{\mathcal{W}}^{\theta}_{\phi_i\rightarrow\phi_f} = \hat{P}_{(\theta,\phi_i)}\hat{P}_{(\theta,\phi_i+\Delta)}\hat{P}_{(\theta,\phi_i+2\Delta)}\cdots\hat{P}_{(\theta,\phi_f)} \tag{9}$$

as the path-order product of the projectors (Eq. (8)) from (θ,ϕ_i) to (θ,ϕ_f) on the sphere, where $\Delta = (\phi_f - \phi_i)/N$ (N is some positive integer). We assume the limit $N \gg 1$ so that [72]

$$\hat{\mathcal{W}}^{\theta}_{\phi_i\rightarrow\phi_f}\left(\hat{\mathcal{W}}^{\theta}_{\phi_i\rightarrow\phi_f}\right)^{\dagger} = \hat{P}_{(\theta,\phi_i)},$$
$$\left(\hat{\mathcal{W}}^{\theta}_{\phi_i\rightarrow\phi_f}\right)^{\dagger}\hat{\mathcal{W}}^{\theta}_{\phi_i\rightarrow\phi_f} = \hat{P}_{(\theta,\phi_f)}. \tag{10}$$

The matrix representation of $\hat{\mathcal{W}}^{\theta}_{\phi_i\rightarrow\phi_f}$ is called the Wilson loop, a 2×2 unitary matrix given by

$$\left(\mathcal{W}^{\theta}_{\phi_i\rightarrow\phi_f}\right)_{mn} = \langle u_{(\theta,\phi_i),m}|\hat{\mathcal{W}}^{\theta}_{\phi_i\rightarrow\phi_f}|u_{(\theta,\phi_f),n}\rangle \tag{11}$$

where $m, n = 1, 2$ is of the occupied states. The Wilson loop here can be understood as a discrete expression of the non-abelian Berry phase [71], which has gauge invariant eigenvalues if the initial point (ϕ_i) coincides with the final point (ϕ_f). We refer to such gauge invariant eigenspectrum as the Wilson spectrum. More specifically, we consider the Wilson loop $\mathcal{W}^{\theta}_{0\rightarrow 2\pi}$ that starts from $(\theta, 0)$ and ends at the same point $(\theta, 2\pi) = (\theta, 0)$. Denote its eigenvalues by $e^{i\chi^{\theta}_n}$ where the phase

$$\chi^{\theta}_n \in [-\pi, \pi) \tag{12}$$

is called the Wilson energy with the label $n = 1, 2$ and θ (polar angle). The plot of χ^{θ}_n against $0 \le \theta \le \pi$ is then referred as the Wilson spectrum, by which we characterize the DN in Fig. 2. Note that the total topological charge of a system must be neutralized since the DNs appear in pairs [48,73]. We found Ref. [74,75] drew a similar conclusion; however, we here approach the problem in a geometrical way by incorporating the Wilson spectrum.

3.5. Discussion

There are debates in the band gap value of β-PbO_2 because an optical gap has been observed in experiments while this material still shows good conductivity. Scanlon and Payne et al. based on the DFT calculation with HSE06 functional, claimed that β-PbO_2 has a direct band gap about 32 meV and argued that such good conductivity is due to the electron doping from the vacancy of oxygen ions [76–79]. Nonetheless, this DFT-calculated band gap of β-PbO_2 is very sensitive to the lattice constant. Since the CB partially consists of the anti-bonding Pb-s orbitals, applying tensile stress will minimize the energy splitting between the bounding and anti-bonding states, which consequently decreases the band gap. We compare the band gap value with different stress using various exchange–correlation functional in Fig. 4a (the band gap is defined as the energy difference between the Γ_6^+ and Γ_7^+ state). Although HSE06 and mBJ functional show a small gap for the experimental lattice constant, they both become gapless after applying tensile stress in c direction, as shown in Fig. 4b and c. Our result indicates that β-PbO_2 may be intrinsic gapless or can become gapless through the applied stress or doping. Similar result, the tunable band gap, is also presented in a previous study on β-PbO_2 [53].

It is worth noting that the topological properties of β-PbO_2 without SOC have been reported in Ref. [53]. In our work, we focus on the SOC case and employ the Wilson loop method on a sphere enclosing

the Dirac node protected by the C4 rotation axis to evaluate the topological mirror Chern number. In this new approach, we classify the topology of the Dirac node itself, and identify the topological charge of ±1 for the Dirac nodes through the Wilson loop method. Moreover, we explore the quadratic behavior of the Dirac bands, analyze the relation between quadratic and linear Dirac bands, and propose to tune the quadratic-to-linear Dirac bands by modifying the SOC strength (see Fig. 2, Supplementary Figures S3, S4, and related discussion). All these in-depth studies are beyond the scope of previous works. On the other hand, in Ref. [55] the Wilson loop method was applied on a mirror plane to evaluate the Z_2 Chern number of PtO_2. This highlights the methodological distinction and the different topological invariants being characterized in the two cases.

Moreover, to emphasize the experimental relevance of our results, we would like to elaborate on suitable techniques to probe the quadratic Dirac node (QDN) and its associated properties. First, the proximity of the QDN to the Fermi level makes it directly accessible by angle-resolved photoemission spectroscopy (ARPES), which can map the band dispersion and distinguish between quadratic and linear dispersions through high-resolution momentum-energy measurements. In particular, a quadratic dispersion will exhibit a parabolic band touching, in contrast to the linear cone-like feature of Dirac fermions [80–83]. Second, scanning tunneling microscopy/spectroscopy (STM/STS) can be employed to probe the local density of states (LDOS). The quadratic dispersion is expected to produce a distinct energy dependence of the LDOS compared to linear Dirac systems, providing a real-space signature of the QDN. Moreover, STM under magnetic fields can resolve Landau level quantization, where quadratic and linear dispersions follow different Landau level scaling relations, enabling clear experimental distinction [82–85]. Third, magneto-transport measurements, such as Shubnikov–de Haas oscillations, can be used to identify the topologically protected Landau levels. The Berry phase and Landau level fan diagram will differ between quadratic and linear band crossings, offering another way to distinguish the two regimes [85,86].

To experimentally tune and enhance the observable effects, introducing stronger spin–orbit coupling (SOC) is a promising route. In the current system, the bands near the Fermi level are dominated by oxygen states, which intrinsically exhibit weak SOC (Supplementary Fig. S4 and related discussion). Therefore, we propose substituting certain amount of oxygen by heavier chalcogen elements such as Se, Te, or Po, which can significantly enhance SOC strength. This modification is expected to (i) stabilize the QDN, (ii) modify the dispersion characteristics, and (iii) potentially induce richer topological phases, thereby facilitating experimental detection. Overall, the combination of ARPES, STM/STS, and magneto-transport measurements, together with SOC engineering via heavy-element substitution, provides a comprehensive and feasible pathway to verify the predicted quadratic Dirac physics and its tunability.

Finally, experimental validation, practical relevance, and potential applications of 3D Dirac semimetals (DSMs) such as Na_3Bi and Cd_3As_2 have been explored. Specifically, Na_3Bi and Cd_3As_2 have been experimentally confirmed to exhibit ultra-high carrier mobilities with Na_3Bi thin films exceeding 7000 cm^2/Vs [87] and Cd_3As_2 demonstrating record-high mobility alongside unique negative magnetoresistance [88]. These results provide direct evidence of the predicted linear electronic dispersions and offer a robust platform for high-efficiency electronic devices. In terms of practical applications, the successful realization of field-effect transistors (FETs) through electrostatic modulation of Na_3Bi films demonstrates the feasibility of solid-state topological devices [87], while the dimensional crossover induced by thinning these materials to a few layers enables a high-temperature quantum spin Hall effect suitable for low-power topological electronics [89]. Furthermore, regarding systems with quadratic Dirac features, the inherent anisotropy of the Fermi surface, characterized by nested ellipsoids as seen in Cd_3As_2 [90], suggests that transport direction can be precisely controlled by manipulating crystallographic orientation or Fermi levels, providing a theoretical foundation for designing directional sensors and logic components in next-generation quantum technologies.

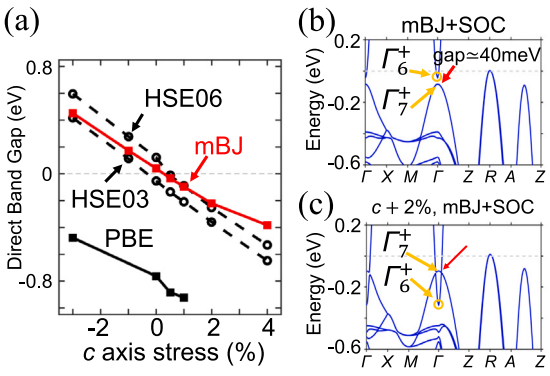

Fig. 4. (a) Calculated band gaps of β-PbO_2 from different functionals versus stress in c axis. (b) (c) The mBJ+SOC band structure using experimental lattice constant with 2% tensile stress in c axis. The group representation at Γ point are denoted by Γ_6^+ and Γ_7^+. Red arrows indicate results from mBJ calculations. (For interpretation of the references to color in this figure legend, the reader is referred to the web version of this article.)

4. Conclusion

In summary, we study electronic structures of β-PbO_2 from first-principles calculations as well as $k\cdot p$ model. We illustrate that the nodal semimetal phase is presented in this material due to the spin-rotational symmetry. We further show that the SOC can open gap along the nodal ring, leading it to a Dirac semimetal. Moreover, the uncommon property: mirror Chern number $n_M = 2$ and anomalous surface state are demonstrated. Beyond previous classification on symmetries of the Dirac semimetals, our work introduces a new type of topological invariance number. On the other hand, β-PbO_2 also exhibits quadratic Dirac semimetal behavior around the Fermi level, which is good for experimental measurements. It is worth noting that this class of topological phase has been predicted but not yet found in real material to date. We demonstrate that the quadratic properties are tunable, which could be realized by doping in the experiment. Previous theoretical works show that quadratic Dirac semimetals have the non-Landau–Fermi liquid properties [43,44]. Owing to the tunable QDN properties, the quantum phase transition from Landau–Fermi liquids to non-Landau–Fermi liquids may be realized in β-PbO_2. Finally, we emphasize that the methodology employed in this work, combining symmetry analysis with Wilson loop calculations, is general, not material-specific, and can be readily applied to other rutile-type materials such as β-PtO_2 as mentioned previously. Our research present a new route to classify gapless topological semimetals and may provide a new method to study the non-Fermi liquid.

CRediT authorship contribution statement

Chin-Shen Kuo: Writing – original draft, Visualization, Methodology, Investigation, Formal analysis. **Angus Huang:** Writing – original draft, Visualization, Methodology, Investigation, Formal analysis. **Chin-Hsuan Chen:** Writing – original draft, Visualization, Methodology. **Horng-Tay Jeng:** Writing – review & editing, Validation, Supervision, Software, Resources, Project administration.

Declaration of competing interest

The authors declare the following financial interests/personal relationships which may be considered as potential competing interests: Horng-Tay Jeng reports a relationship with National Science and Technology Council that includes: funding grants. If there are other authors, they declare that they have no known competing financial interests or personal relationships that could have appeared to influence the work reported in this paper.

Acknowledgments

This work was supported by the National Science and Technology Council, Taiwan. (Grant number: NSTC 112-2112-M-007 -034 -MY3) H.-T.J. thanks support from NCHC, Taiwan, CINC-NTU, Taiwan, AS-iMATE-111-12, and CQT-NTHU-MOE, Taiwan.

Appendix A. Supplementary data

Supplementary material related to this article can be found online at https://doi.org/10.1016/j.mtadv.2026.100805.

Data availability

No data was used for the research described in the article.

References

[1] S.-M. Huang, et al., A Weyl Fermion semimetal with surface Fermi arcs in the transition metal monopnictide TaAs class, Nat. Commun. 6 (2015) 7373.
[2] H. Weng, C. Fang, Z. Fang, B.A. Bernevig, X. Dai, Weyl semimetal phase in noncentrosymmetric transition-metal monophosphides, Phys. Rev. X 5 (2015) 011029.
[3] B.Q. Lv, et al., Experimental discovery of Weyl semimetal TaAs, Phys. Rev. X 5 (2015) 031013.
[4] S.-Y. Xu, et al., Discovery of a Weyl fermion semimetal and topological Fermi arcs, Science 349 (6248) (2015) 613.
[5] Z. Wang, H. Weng, Q. Wu, X. Dai, Z. Fang, Three-dimensional Dirac semimetal and quantum transport in Cd_3As_2, Phys. Rev. B 88 (2013) 125427.
[6] S. Borisenko, Q. Gibson, D. Evtushinsky, V. Zabolotnyy, B. Büchner, R.J. Cava, Experimental realization of a three-dimensional Dirac semimetal, Phys. Rev. Lett. 113 (2014) 027603.
[7] Z.K. Liu, et al., A stable three-dimensional topological Dirac semimetal Cd3As2, Nat. Mater. 13 (7) (2014) 677.
[8] M. Neupane, et al., Observation of a three-dimensional topological Dirac semimetal phase in high-mobility Cd3As2, Nat. Commun. 5 (2014) 3786.
[9] T. Liang, Q. Gibson, M.N. Ali, M. Liu, R.J. Cava, N.P. Ong, Ultrahigh mobility and giant magnetoresistance in the Dirac semimetal?Cd3As2, Nat. Mater. 14 (3) (2015) 280.
[10] Z. Wang, Y. Sun, X.-Q. Chen, C. Franchini, G. Xu, H. Weng, X. Dai, Z. Fang, Dirac semimetal and topological phase transitions in A_3Bi (A = Na, K, Rb), Phys. Rev. B 85 (2012) 195320.
[11] Z.K. Liu, et al., Discovery of a three-dimensional topological Dirac semimetal, Na3Bi, Science 343 (6173) (2014) 864.
[12] S.-Y. Xu, et al., Observation of Fermi arc surface states in a topological metal, Science 347 (6219) (2015) 294.
[13] P. Tang, Q. Zhou, G. Xu, S.-C. Zhang, Dirac fermions in an antiferromagnetic semimetal, Nat. Phys. 12 (2016) 1100.
[14] D.M. Nenno, C.A.C. Garcia, J. Gooth, C. Felser, P. Narang, Axion physics in condensed-matter systems, Nat. Rev. Phys. 2 (2020) 682.
[15] L. Fu, C.L. Kane, Superconducting proximity effect and majorana Fermions at the surface of a topological insulator, Phys. Rev. Lett. 100 (2008) 096407.
[16] V. Mourik, K. Zuo, S.M. Frolov, S.R. Plissard, E.P.A.M. Bakkers, L.P. Kouwenhoven, Signatures of majorana Fermions in hybrid superconductor-semiconductor nanowire devices, Science 336 (6084) (2012) 1003.
[17] Q.L. He, et al., Chiral majorana fermion modes in a quantum anomalous hall insulator–superconductor structure, Science 357 (6348) (2017) 294.
[18] S. Nadj-Perge, et al., Observation of majorana fermions in ferromagnetic atomic chains on a superconductor, Science 346 (6209) (2014) 602.
[19] S.-Y. Guan, et al., Superconducting topological surface states in the noncentrosymmetric bulk superconductor PbTaSe2, Sci. Adv. 2 (11) (2016) e1600894.
[20] L. Huang, et al., Spectroscopic evidence for a type II Weyl semimetallic state in MoTe2, Nat. Mater. 15 (11) (2016) 1155.
[21] A.A. Soluyanov, D. Gresch, Z. Wang, Q. Wu, M. Troyer, X. Dai, B.A. Bernevig, Type-II Weyl semimetals, Nature 527 (7579) (2015) 495.
[22] K. Deng, et al., Experimental observation of topological Fermi arcs in type-II Weyl semimetal MoTe2, Nat. Phys. 12 (2016) 1105.
[23] T.-R. Chang, et al., Prediction of an arc-tunable Weyl Fermion metallic state in MoxW1-xTe2, Nat. Commun. 7 (2016) 10639.
[24] H.-J. Noh, J. Jeong, E.-J. Cho, K. Kim, B.I. Min, B.-G. Park, Experimental realization of type-II Dirac Fermions in a $PdTe_2$ superconductor, Phys. Rev. Lett. 119 (2017) 016401.
[25] F. Fei, et al., Nontrivial berry phase and type-II Dirac transport in the layered material $PdTe_2$, Phys. Rev. B 96 (2017) 041201.
[26] T.-R. Chang, et al., Type-II symmetry-protected topological Dirac semimetals, Phys. Rev. Lett. 119 (2017) 026404.
[27] G. Bian, et al., Drumhead surface states and topological nodal-line fermions in $TlTaSe_2$, Phys. Rev. B 93 (2016) 121113.
[28] G. Bian, et al., Topological nodal-line fermions in spin-orbit metal PbTaSe2, Nat. Commun. 7 (2016) 10556.
[29] C. Fang, Y. Chen, H.-Y. Kee, L. Fu, Topological nodal line semimetals with and without spin-orbital coupling, Phys. Rev. B 92 (2015) 081201.
[30] C. Fang, H. Weng, X. Dai, Z. Fang, Topological nodal line semimetals, Chin. Phys. B 25 (11) (2016) 117106.
[31] A.A. Burkov, M.D. Hook, L. Balents, Topological nodal semimetals, Phys. Rev. B 84 (2011) 235126.
[32] B. Bradlyn, J. Cano, Z. Wang, M.G. Vergniory, C. Felser, R.J. Cava, B.A. Bernevig, Beyond Dirac and Weyl fermions: Unconventional quasiparticles in conventional crystals, Science 353 (6299) (2016) 558.
[33] G. Chang, et al., Nexus fermions in topological symmorphic crystalline metals, Sci. Rep. 7 (1) (2017) 1688.
[34] H. Weng, C. Fang, Z. Fang, X. Dai, Topological semimetals with triply degenerate nodal points in θ-phase tantalum nitride, Phys. Rev. B 93 (2016) 241202.
[35] Z. Zhu, G.W. Winkler, Q. Wu, J. Li, A.A. Soluyanov, Triple point topological metals, Phys. Rev. X 6 (2016) 031003.
[36] G.W. Winkler, Q. Wu, M. Troyer, P. Krogstrup, A.A. Soluyanov, Topological phases in $InAs_{1-x}Sb_x$: From novel topological semimetal to majorana wire, Phys. Rev. Lett. 117 (2016) 076403.
[37] T. Hyart, T.T. Heikkilä, Momentum-space structure of surface states in a topological semimetal with a nexus point of Dirac lines, Phys. Rev. B 93 (2016) 235147.
[38] B.Q. Lv, et al., Observation of three-component fermions in the topological semimetal molybdenum phosphide, Nature 546 (7660) (2017) 627.
[39] C. Fang, M.J. Gilbert, X. Dai, B.A. Bernevig, Multi-Weyl topological semimetals stabilized by point group symmetry, Phys. Rev. Lett. 108 (2012) 266802.
[40] G. Xu, H. Weng, Z. Wang, X. Dai, Z. Fang, Chern semimetal and the quantized anomalous hall effect in HgCr2Se4, Phys. Rev. Lett. 107 (2011) 186806.
[41] S.-M. Huang, et al., New type of Weyl semimetal with quadratic double Weyl fermions, Proc. Natl. Acad. Sci. USA 113 (5) (2016) 1180.
[42] T.-R. Chang, S.-Y. Xu, D.S. Sanchez, W.-F. Tsai, S.-M. Huang, G. Chang, C.-H. Hsu, G. Bian, I. Belopolski, Z.-M. Yu, S.A. Yang, T. Neupert, H.-T. Jeng, H. Lin, M.Z. Hasan, Type-II symmetry-protected topological Dirac semimetals, Phys. Rev. Lett. 119 (2) (2017) 026404.
[43] E.-G. Moon, C. Xu, Y.B. Kim, L. Balents, Non-Fermi-liquid and topological states with strong spin-orbit coupling, Phys. Rev. Lett. 111 (2013) 206401.
[44] B.-J. Yang, N. Nagaosa, Classification of stable three-dimensional Dirac semimetals with nontrivial topology, Nat. Commun. 5 (2014) 4898.
[45] Q. Liu, A. Zunger, Predicted realization of cubic Dirac Fermion in quasi-one-dimensional transition-metal monochalcogenides, Phys. Rev. X 7 (2017) 021019.
[46] W. Wu, Z.-M. Yu, X. Zhou, Y.X. Zhao, S.A. Yang, Higher-order Dirac fermions in three dimensions, Phys. Rev. B 101 (20) (2020) 205134.
[47] B.-J. Yang, N. Nagaosa, Classification of stable three-dimensional Dirac semimetals with nontrivial topology, Nat. Commun. 5 (4898) (2014) 1–10.
[48] Z. Wang, Y. Sun, X.-Q. Chen, C. Franchini, G. Xu, H. Weng, X. Dai, Z. Fang, Dirac semimetal and topological phase transitions in A3Bi (A=Na, K, Rb), Phys. Rev. B 85 (2012) 195320.
[49] C.-H. Hsu, X. Zhou, T.-R. Chang, Q. Ma, N. Gedik, A. Bansil, S.-Y. Xu, H. Lin, L. Fu, Topology on a new facet of bismuth, Proc. Natl. Acad. Sci. USA 116 (27) (2019) 13255–13259.
[50] J.-Z. Ma, S.-N. Zhang, J.P. Song, Q.-S. Wu, S.A. Ekahana, M. Naamneh, M. Radovic, V.N. Strocov, S.-Y. Gao, T. Qian, H. Ding, K. He, K. Manna, C. Felser, N.C. Plumb, O.V. Yazyev, Y.-M. Xiong, M. Shi, Giant chern number of a Weyl nodal surface without upper limit, Phys. Rev. B 105 (2022) 115118.
[51] C. Fang, M.J. Gilbert, X. Dai, B.A. Bernevig, Multi-Weyl topological semimetals stabilized by point group symmetry, Phys. Rev. Lett. 108 (2012) 266802.
[52] S. Mahatara, B. Kiefer, Does β-PbO2 harbor topological states? J. Phys.: Condens. Matter. 32 (25) (2020) 255504.
[53] B. Peng, I. Bravić, J.L. MacManus-Driscoll, et al., Topological semimetallic phase in PbO_2 promoted by temperature, Phys. Rev. B 100 (16) (2019) 161101.
[54] B.J. Wieder, Z. Wang, J. Cano, X. Dai, L.M. Schoop, B. Bradlyn, B.A. Bernevig, Strong and fragile topological Dirac semimetals with higher-order Fermi arcs, Nat. Commun. 11 (627) (2020) 1–13.
[55] R. Kim, B.-J. Yang, C.H. Kim, Crystalline topological Dirac semimetal phase in rutile structure β'–PtO_2, Phys. Rev. B 99 (4) (2019) 045130.
[56] G. Kresse, J. Hafner, Ab initio, Phys. Rev. B 48 (1993) 13115.
[57] G. Kresse, J. Furthmüller, Efficient iterative schemes for ab initio total-energy calculations using a plane-wave basis set, Phys. Rev. B 54 (1996) 11169.
[58] G. Kresse, J. Furthmüller, Efficiency of ab-initio total energy calculations for metals and semiconductors using a plane-wave basis set, Comput. Mater. Sci. 6 (1) (1996) 15.
[59] J.P. Perdew, K. Burke, M. Ernzerhof, Generalized gradient approximation made simple, Phys. Rev. Lett. 77 (1996) 3865.

[60] J. Heyd, G.E. Scuseria, M. Ernzerhof, Hybrid functionals based on a screened Coulomb potential, J. Chem. Phys. 118 (18) (2003) 8207.
[61] J. Heyd, G.E. Scuseria, M. Ernzerhof, Erratum: "hybrid functionals based on a screened Coulomb potential" [J. Chem. Phys. 118, 8207 (2003)], J. Chem. Phys. 124 (21) (2006) 219906.
[62] A.V. Krukau, O.A. Vydrov, A.F. Izmaylov, G.E. Scuseria, Influence of the exchange screening parameter on the performance of screened hybrid functionals, J. Chem. Phys. 125 (22) (2006) 224106.
[63] A.D. Becke, E.R. Johnson, A simple effective potential for exchange, J. Chem. Phys. 124 (22) (2006) 221101.
[64] F. Tran, P. Blaha, Accurate band gaps of semiconductors and insulators with a semilocal exchange-correlation potential, Phys. Rev. Lett. 102 (2009) 226401.
[65] H. Zhang, C.-X. Liu, X.-L. Qi, X. Dai, Z. Fang, S.-C. Zhang, Topological insulators in Bi2Se3, Bi2Te3 and Sb2Te3 with a single Dirac cone on the surface, Nat. Phys. 5 (2009) 438.
[66] H. Singh, M. Singh, S. Kumar, M.K. Kashyap, Full potential calculation of electronic properties of rutile RO_2 (R = Si, Ge, Sn and Pb) compounds via modified Becke Johnson potential, Phys. B 406 (20) (2011) 3825.
[67] Y. Kim, B.J. Wieder, C.L. Kane, A.M. Rappe, Dirac line nodes in inversion-symmetric crystals, Phys. Rev. Lett. 115 (2015) 036806.
[68] A. Alexandradinata, Z. Wang, B.A. Bernevig, Topological insulators from group cohomology, Phys. Rev. X 6 (2016) 021008.
[69] A. Alexandradinata, B.A. Bernevig, Berry-phase description of topological crystalline insulators, Phys. Rev. B 93 (2016) 205104.
[70] B.J. Wieder, B. Bradlyn, Z. Wang, J. Cano, Y. Kim, H.-S.D. Kim, A.M. Rappe, C.L. Kane, B.A. Bernevig, Wallpaper Fermions and the topological Dirac insulator, 2017, arXiv:1705.01617. arXiv preprint.
[71] R. Yu, X.L. Qi, A. Bernevig, Z. Fang, X. Dai, Equivalent expression of Z2 topological invariant for band insulators using the non-Abelian Berry connection, Phys. Rev. B 84 (2011) 075119.
[72] D. Varjas, F. de Juan, Y.-M. Lu, Space group constraints on weak indices in topological insulators, 2016, arXiv:1603.04450.
[73] Z. Wang, H. Weng, Q. Wu, X. Dai, Z. Fang, Three-dimensional Dirac semimetal and quantum transport in Cd3As2, Phys. Rev. B 88 (2013) 125427.
[74] B.-J. Yang, T. Morimoto, A. Furusaki, Topological charges of three-dimensional Dirac semimetals with rotation symmetry, Phys. Rev. B 92 (2015) 165120.
[75] S. Kobayashi, M. Sato, Topological superconductivity in Dirac semimetals, Phys. Rev. Lett. 115 (2015) 187001.
[76] D.O. Scanlon, A.B. Kehoe, G.W. Watson, M.O. Jones, W.I.F. David, D.J. Payne, R.G. Egdell, P.P. Edwards, A. Walsh, Nature of the band gap and origin of the conductivity of PbO_2 revealed by theory and experiment, Phys. Rev. Lett. 107 (2011) 246402.
[77] D.J. Payne, R.G. Egdell, W. Hao, J.S. Foord, A. Walsh, G.W. Watso, Why is lead dioxide metallic? Chem. Phys. Lett. 411 (1) (2005) 181.
[78] D.J. Payne, R.G. Egdell, D.S.L. Law, P.-A. Glans, T. Learmonth, K.E. Smith, J. Guo, A. Walsh, G.W. Watson, Experimental and theoretical study of the electronic structures of [small alpha]-PbO and [small beta]-PbO2, J. Mater. Chem. 17 (2007) 267.
[79] D.J. Payne, et al., Nature of electronic states at the Fermi level of metallic $\beta-PbO_2$ revealed by hard x-ray photoemission spectroscopy, Phys. Rev. B 75 (2007) 153102.
[80] R. Sankar, G. Peramaiyan, I.P. Muthuselvam, C.J. Butler, K. Dimitri, M. Neupane, G.N. Rao, M.-T. Lin, F.C. Chou, Crystal growth of Dirac semimetal ZrSiS with high magnetoresistance and mobility, Sci. Rep. 7 (40603) (2017) 40603.
[81] Y. Yen, C.-L. Chiu, P.-H. Lin, R. Sankar, T.-M. Chuang, G.-Y. Guo, Dirac nodal line and Rashba spin-split surface states in nonsymmorphic ZrGeTe, New J. Phys. 23 (10) (2021) 103019.
[82] N. Valadez, I.B. Elius, D. James, P. Radanovich, T. Romanova, S. Elgalal, G. Chajewski, F. Mesple, E. Thompson, K.T. Chu, M. Yankowitz, A. Ptok, D. Kaczorowski, M. Neupane, Low-lying electronic structure of the rare earth based topological nodal line semimetal candidate DySbTe, Phys. Rev. B 112 (15) (2025) 155148.
[83] C.E. Matt, H. Pirie, A. Soumyanarayanan, Y. He, M.M. Yee, P. Chen, Y. Liu, D.T. Larson, W.S. Paz, J.J. Palacios, M.H. Hamidian, J.E. Hoffman, Consistency between ARPES and STM measurements on SmB_6, Phys. Rev. B 101 (8) (2020) 085142.
[84] L. Jiao, Q.N. Xu, Y.P. Qi, S.-C. Wu, Y. Sun, C. Felser, S. Wirth, Observation of Landau quantization and standing waves in HfSiS, Phys. Rev. B 97 (19) (2018) 195137.
[85] E.Y. Andrei, G. Li, X. Du, Electronic properties of graphene: A perspective from scanning tunneling microscopy and magnetotransport, Rep. Progr. Phys. 75 (5) (2012) 056501.
[86] A.S. Wadge, P.K. Tanwar, G. Cuono, C. Autieri, Nodal-line semimetals: Emerging opportunities for topological electronics and beyond, 2026, http://dx.doi.org/10.48550/arXiv.2604.00596, arXiv arXiv:2604.00596.
[87] J. Hellerstedt, I. Yudhistira, M.T. Edmonds, C. Liu, J. Collins, S. Adam, M.S. Fuhrer, Electrostatic modulation of the electronic properties of Dirac semimetal Na_3Bi thin films, Phys. Rev. Mater. 1 (5) (2017) 054203.
[88] H. Li, H. He, H.-Z. Lu, H. Zhang, H. Liu, R. Ma, Z. Fan, S.-Q. Shen, J. Wang, Negative magnetoresistance in Dirac semimetal Cd3As2, Nat. Commun. 7 (10301) (2016) 10301.
[89] H. Xia, Y. Li, M. Cai, L. Qin, N. Zou, L. Peng, W. Duan, Y. Xu, W. Zhang, Y.-S. Fu, Dimensional crossover and topological phase transition in Dirac semimetal Na3Bi films, ACS Nano 13 (8) (2019) 9647–9654.
[90] Y. Zhao, H. Liu, C. Zhang, H. Wang, J. Wang, Z. Lin, Y. Xing, H. Lu, J. Liu, Y. Wang, S.M. Brombosz, Z. Xiao, S. Jia, X.C. Xie, J. Wang, Anisotropic Fermi surface and quantum limit transport in high mobility three-dimensional Dirac semimetal Cd_3As_2, Phys. Rev. X 5 (3) (2015) 031037.